CLIMATOLOGY

Direct and seasonal legacy effects of the 2018 heat wave and drought on European ecosystem productivity

A. Bastos[1]*†, P. Ciais[2], P. Friedlingstein[3,4], S. Sitch[5], J. Pongratz[1,6], L. Fan[7], J. P. Wigneron[7], U. Weber[8], M. Reichstein[8], Z. Fu[2], P. Anthoni[9], A. Arneth[9], V. Haverd[10], A. K. Jain[11], E. Joetzjer[12], J. Knauer[10], S. Lienert[13], T. Loughran[1], P. C. McGuire[14], H. Tian[15], N. Viovy[2], S. Zaehle[8]

Copyright © 2020 The Authors, some rights reserved; exclusive licensee American Association for the Advancement of Science. No claim to original U.S. Government Works. Distributed under a Creative Commons Attribution NonCommercial License 4.0 (CC BY-NC).

In summer 2018, central and northern Europe were stricken by extreme drought and heat (DH2018). The DH2018 differed from previous events in being preceded by extreme spring warming and brightening, but moderate rainfall deficits, yet registering the fastest transition between wet winter conditions and extreme summer drought. Using 11 vegetation models, we show that spring conditions promoted increased vegetation growth, which, in turn, contributed to fast soil moisture depletion, amplifying the summer drought. We find regional asymmetries in summer ecosystem carbon fluxes: increased (reduced) sink in the northern (southern) areas affected by drought. These asymmetries can be explained by distinct legacy effects of spring growth and of water-use efficiency dynamics mediated by vegetation composition, rather than by distinct ecosystem responses to summer heat/drought. The asymmetries in carbon and water exchanges during spring and summer 2018 suggest that future land-management strategies could influence patterns of summer heat waves and droughts under long-term warming.

Downloaded from http://advances.sciencemag.org/ on July 27, 2020

INTRODUCTION

In the past two decades, Europe has been stricken by major summer heat waves and drought, with heavy impacts on food production, public health, air pollution, and ecosystem carbon uptake (*1*–*3*). For instance, the drought-heat events of 2003 and 2010 in central Europe and western Russia, respectively (referred to here as DH2003 and DH2010), broke, at the time, the >500-year-long summer temperature record over the continent (*1*). While these events were exceptional at the time, their likelihood will increase in the coming century due to anthropogenic global warming (*1*). In 2018, the European summer land temperature anomaly broke the record yet again, although with distinct spatiotemporal patterns (*4*). The 2018 summer was characterized by extreme drought in central and northern Europe (Fig. 1A, referred to, for consistency, as DH2018), with several countries suffering major economic costs from crop failure. Compensations to farmers from crop losses due to drought in 2018 reached €340 million in Germany and €116 million in Sweden (*5*).

Several studies have shown that both DH2003 and DH2010 resulted in strong reductions in vegetation productivity due to soil moisture (SM) deficits, high water vapor pressure and heat stress, increases in ecosystem respiration, and increased fire activity, leading to a reduction of the net CO_2 uptake in ecosystems (*2*, *6*, *7*). The SM deficits associated with summer heat waves seem to explain most of the decrease in productivity in DH2003 (*2*, *8*) and, to a smaller extent, in DH2010 (*9*, *10*). Some ecosystems affected by DH2010 showed, however, increased summer productivity, possibly because high temperatures in 2010 were still favorable for vegetation growth, especially in higher latitudes (*9*). Differences in impacts of summer heat and drought on ecosystems may also be related with different trajectories in water-use efficiency (WUE; i.e., unit of carbon gained through photosynthesis per unit of water lost through transpiration) over the growing season (*8*). In DH2003 and DH2010, grasslands and croplands were more strongly hit than forests, because forests have deep-water access, and are also more conservative in the use of water over the growing season (*9*, *11*, *12*).

While several studies have analyzed the impacts of DH events resulting from concurrent SM deficits, heat stress, and fire activity (direct impacts) on ecosystems' carbon balance, less attention has been devoted to the influence of preceding climate conditions in the ecosystems' response to the summer extremes (legacy effects). All three DH events in Europe were preceded by warm springs, with reduced rainfall and sunnier conditions. The climate anomalies in spring can affect the annual carbon balance by (i) directly affecting ecosystem productivity, (ii) altering the water and energy balance in the following seasons due to land-atmosphere feedbacks, and (iii) affecting the response of ecosystems to climate anomalies in subsequent seasons by altering their baseline state. Warm and sunny conditions in early spring directly result in earlier vegetation green-up and growth, which might partly compensate for the summer productivity losses from drought and extreme heat (*9*, *13*). However, spring climate conditions can have different legacy effects to the summer and annual carbon balance. Previous studies have highlighted the role of spring precipitation deficits, increased solar radiation and warming in amplifying the high temperature anomalies in

[1]Department of Geography, Ludwig Maximilian University of Munich, Munich, Luisenstr. 37, 80333 Munich, Germany. [2]Laboratoire des Sciences du Climat et de l'Environnement (LSCE), CEA-CNRS-UVSQ, UMR8212, 91191 Gif-sur-Yvette, France. [3]College of Engineering, Mathematics and Physical Sciences, University of Exeter, Exeter EX4 4QF, UK. [4]LMD/IPSL, ENS, PSL Université, École Polytechnique, Institut Polytechnique de Paris, Sorbonne Université, CNRS, Paris, France. [5]College of Life and Environmental Sciences, University of Exeter, Exeter EX4 4RJ, UK. [6]Max Planck Institute for Meteorology, 20146 Hamburg, Germany. [7]ISPA, UMR 1391, INRA Nouvelle-Aquitaine, Université de Bordeaux, Grande Ferrage, Villenave d'Ornon, France. [8]Max Planck Institute for Biogeochemistry, 07745 Jena, Germany. [9]Karlsruhe Institute of Technology, Institute of Meteorology and Climate Research/Atmospheric Environmental Research, 82467 Garmisch-Partenkirchen, Germany. [10]CSIRO Oceans and Atmosphere, Canberra, ACT 2601, Australia. [11]Department of Atmospheric Sciences, University of Illinois, Urbana, IL 61801, USA. [12]CNRM, Université de Toulouse, Météo-France, CNRS, Toulouse, France. [13]Climate and Environmental Physics, Physics Institute and Oeschger Centre for Climate Change Research, University of Bern, Bern CH-3012, Switzerland. [14]Department of Meteorology, Department of Geography & Environmental Science, and National Centre for Atmospheric Science, University of Reading, Earley Gate, RG66BB Reading, UK. [15]International Center for Climate and Global Change Research, School of Forestry and Wildlife Sciences, Auburn University, 602 Duncan Drive, Auburn, AL 36849, USA.
*Present address: Max Planck Institute for Biogeochemistry, 00745 Jena, Germany.
†Corresponding author. Email: abastos@bgc-jena.mpg.de

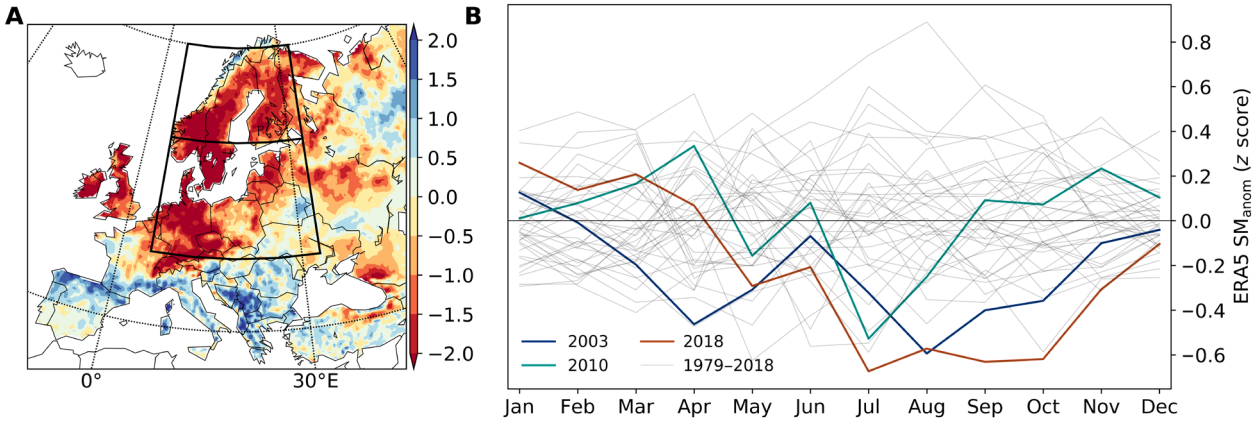

Fig. 1. Drought patterns in summer 2018. (**A**) Spatial distribution of SM anomaly (SM_{anom}) from ERA5 fields (see Materials and Methods) in summer (JJA) and (**B**) distribution of seasonal SM_{anom} at continental scale for the study period 1979–2018 (gray lines) and the corresponding trajectories in 2003, 2010, and 2018. Continental Europe refers to the domain within 32°N and 75°N and −11°E and 65°E.

extreme summers in Europe due to SM depletion (*1*, *6*, *14*), and thereby the impact of summer on ecosystem productivity. Increased spring growth may also negatively affect the ecosystem carbon balance in summer or autumn if the additional biomass cannot be sustained (e.g., due to summer drought), by increasing plant respiration and by SM depletion from increased evapotranspiration (ET). Reduced SM could reduce assimilation and maintenance respiration in summer and limit heterotrophic respiration, but increased soil temperatures also lead to increased heterotrophic respiration. Furthermore, spring drought and warming might contribute to increased summer fire activity through higher fuel loads and more flammable fuel. Whether early drought amplifies carbon losses in summer would depend on the net of these effects. A question that remains open is to what extent the earlier vegetation growth in response to increased radiation and warming in spring contributes to earlier SM depletion, possibly amplifying subsequent carbon losses (*15*).

Each of the recent extreme heat and drought events in Europe provides a unique opportunity to study the response of ecosystems to heat and drought events and evaluate how they affect the terrestrial carbon cycle. The extreme spring warming in 2018 is a good case study to assess seasonal legacy and compensation effects from warm springs in ecosystem water and carbon exchanges. Here, we focus our analysis on geographic Europe including western Russia (32°N to 75°N and −11°E to 65°E) and perform a set of factorial simulations with a group of 11 dynamic global vegetation models (DGVMs) to (i) quantify the anomalies in carbon fluxes during spring and summer in 2018, (ii) evaluate possible seasonal compensation effects between spring and summer responses to 2018 climate anomalies, and (iii) identify the seasonal legacy effects of spring and summer climate to the SM and carbon exchange anomalies during DH2018 event and over 2018.

RESULTS

Features of the 2018 drought and heat event

In 2018, Germany, southern Scandinavia, the United Kingdom, and Ireland registered extreme summer agricultural drought, given by SM anomalies (SM_{anom}) from the ERA5 reanalysis (see Materials and Methods) in June to August (JJA) (Fig. 1A). Severe drought affected most of central and eastern European countries and Scandinavia. For different definitions of extreme drought (see Materials and Methods), 2018 registered the largest extent affected by extreme drought (24 to 38 Mha) compared to 2003 (20 to 28 Mha) and 2010 (14 to 18 Mha). Severe drought affected 23 to 44 Mha in 2018 compared to 19 to 45 Mha in 2003 and 18 to 38 Mha in 2010.

For most regions, severe or extreme summer drought co-occurred with warmer and drier than average summer conditions and increased solar radiation, relative to the 1979–2018 record, although summer temperature anomalies were generally not as strong as in 2003 and 2010 (fig. S1). Record-high summer temperature and radiation and record-low summer rainfall were mainly confined to central Europe (fig. S1). Compared to other years in the 40-year-long record, though, 2018 registered the strongest transition between a wet winter/spring and dry summer/autumn at continental scale (Fig. 1B). At continental scale, DH2003, DH2010, and DH2018 were all preceded by wetter-than-average winters (positive SM_{anom}) and by sharp decreases in SM from spring to summer. Still, March and April 2018 corresponded to the highest SM_{anom} during 1979–2018, while July to August were comparable to DH2003 and DH2010, and from September onward 2018 had the lowest SM_{anom} on record. Such sharp enhancement in drought conditions during and after late spring 2018 is likely related to the extremely high spring [March-April-May (MAM)] temperature anomalies registered in Germany and Eastern Europe, as well as precipitation deficits—though generally not extreme—along with extremely high solar radiation in Scandinavia and eastern Europe (fig. S2). This extreme spring warming and brightening is a distinctive feature of 2018, higher than the corresponding spring anomalies in the regions affected by DH2003 and DH2010.

Seasonal anomalies in carbon fluxes

The spatial distribution of total SM_{anom} simulated by the multimodel ensemble median (MMEM; the median reduces the influence of few outliers) of 11 DGVMs (Materials and Methods) shows good agreement with surface SM_{anom} measured by passive microwave sensors from the SMOS (Soil Moisture and Ocean Salinity) satellite (Materials and Methods) with SM_{anom} patterns (fig. S3). This indicates that the ensemble of DGVMs can overall simulate well the agricultural drought conditions in summer 2018.

Downloaded from http://advances.sciencemag.org/ on July 27, 2020

According to the DGVM MMEM, spring 2018 was associated with positive net biome production (NBP) anomalies (defined positive for above-average CO_2 uptake) over most of Europe of about 5 to 10 gC m^{-2} $month^{-1}$ (Fig. 2A). Record-high CO_2 uptake was estimated in several regions in southern (Balkans, Turkey) and northern (western Russia, Scandinavia, and Baltic countries) Europe. In summer, the NBP anomalies were more spatially heterogeneous, with negative NBP anomalies extending over a region encompassing western and central Europe and western Russia registering below average CO_2 uptake (Fig. 2B), but positive NBP anomalies estimated in Scandinavia and in southern Europe. Central Europe and southern Sweden registered record-low sinks, with CO_2 uptake dropping by more than 50% (−30 gC m^{-2} $month^{-1}$) but not strong enough to turn ecosystems into absolute sources. Positive NBP anomalies in the south are most pronounced in those regions with wetter summer conditions, while those in the north are collocated with strong drought (Fig. 1A).

To confirm general DGVM performance, we analyzed satellite-based estimates of satellite vegetation optical depth in the microwave L-band (L-VOD; Materials and Methods). L-VOD standardized changes were calculated from aggregated L-VOD for spring and summer months from 2010 to 2018 (fig. S3) and reflect changes in aboveground biomass carbon. Negative L-VOD changes dominate the region extending from northwestern France to eastern Poland and the Baltic countries, as well as southern Scandinavia, while L-VOD increase is found in central and northern Scandinavia, northwestern Russia, and most of southern Europe. When compared with simulated anomalies for NBP minus soil respiration for the same reference period and the same months, L-VOD changes show good agreement with DGVM estimates (fig. S3).

The positive NBP anomalies in spring and summer generally match those of gross primary production (GPP); (fig. S4). In spring, DGVMs estimate widespread GPP increase and record-high values in Scandinavia and southern Europe. These patterns are generally consistent with GPP estimates from the data-driven product FLUXCOM (fig. S5) (*16*), although FLUXCOM additionally estimates record-high spring GPP in central Germany. In summer, regions with negative (positive) NBP anomalies are associated with below (above) average GPP, and most of the regions with extremely high or extremely low NBP match regions with record GPP anomalies. An exception is found in eastern Europe and Baltic countries, where DGVMs estimate below-average NBP during summer, but enhanced or close to average vegetation productivity. This is due to a strong contribution of total ecosystem respiration (TER) and, to a lesser extent, of fires (fig. S4). FLUXCOM also points to positive GPP anomalies in eastern Europe but in a smaller sector and a larger region with decreased summer TER (fig. S5). These differences suggest a possible oversensitivity of GPP from DGVMs to the alleviation of rainfall deficits during summer in those regions (fig. S1).

Our results indicate an asymmetry in the summer carbon flux anomalies, with the northern sector of the drought-affected region showing increased NBP and GPP during summer, while the southern sector registered strong decreases in both variables. This asymmetry may be due to distinct responses of ecosystems to summer warming and drying but also from different legacy effects from spring climate conditions to summer water and carbon fluxes (Materials and Methods). To understand this asymmetry, we divide the region affected by DH2018 in two sectors: R1 (southern sector of DH2018, reduced summer CO_2 uptake) and R2 (northern sector of DH2018, increased summer CO_2 uptake).

Direct and legacy impacts of spring and summer climate to continental net CO_2 uptake

Based on the three idealized simulations (reference, S_{Ref}, spring effects, S_{MAM}, and summer effects, S_{JJA}; see Materials and Methods), we find strong differences between the individual impacts of each season on carbon fluxes (Fig. 3, A and B) and the seasonal anomalies described above (Fig. 2).

The spring-related NBP anomalies (Fig. 3A) largely reflect a positive correlation with temperature and radiation anomalies, with increased uptake confined to central and northern Europe and Turkey. In most of western Europe, DGVMs estimate a direct negative effect of spring

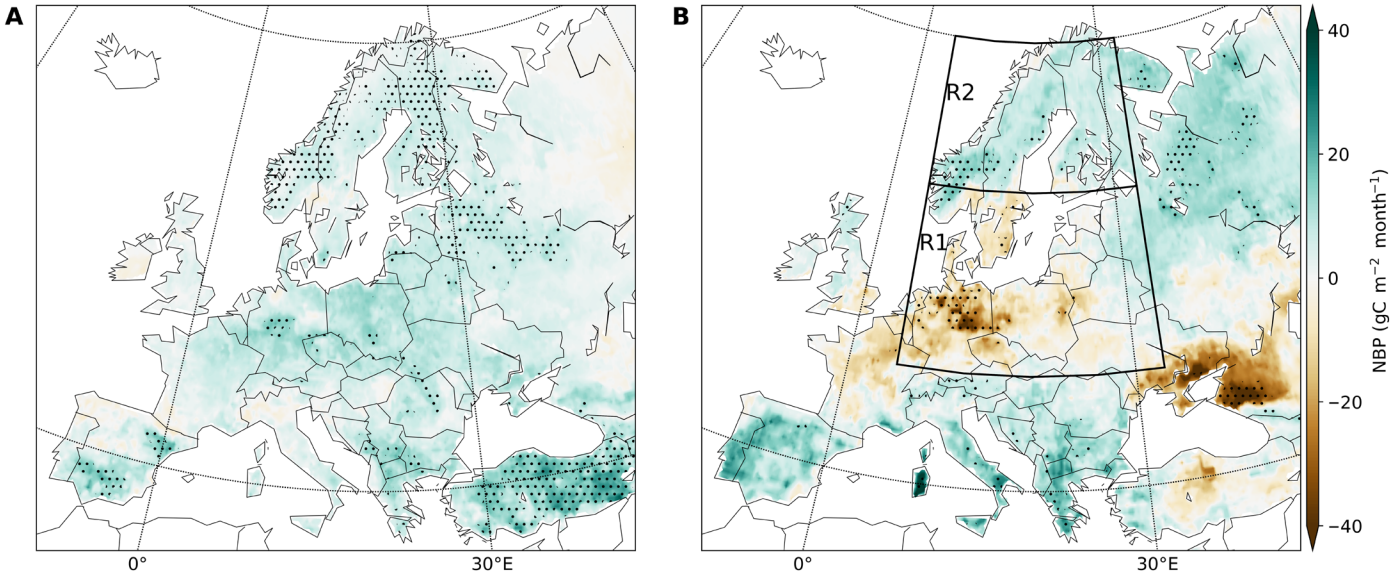

Fig. 2. Anomalies of CO_2 fluxes during spring and summer 2018. Spatial patterns of NBP anomalies (reference period 1979–2018) during (**A**) spring (MAM) and (**B**) summer (JJA) 2018 estimated by the MMEM of 11 DGVMs. A positive (negative) value indicates higher (lower) net CO_2 uptake than the 40-year average. The color map shows the multimodel ensemble mean anomalies, and the stippling indicates those regions with extremely low (rank 40th) or extremely high (rank 1st) values over the reference period.

Downloaded from http://advances.sciencemag.org/ on July 27, 2020

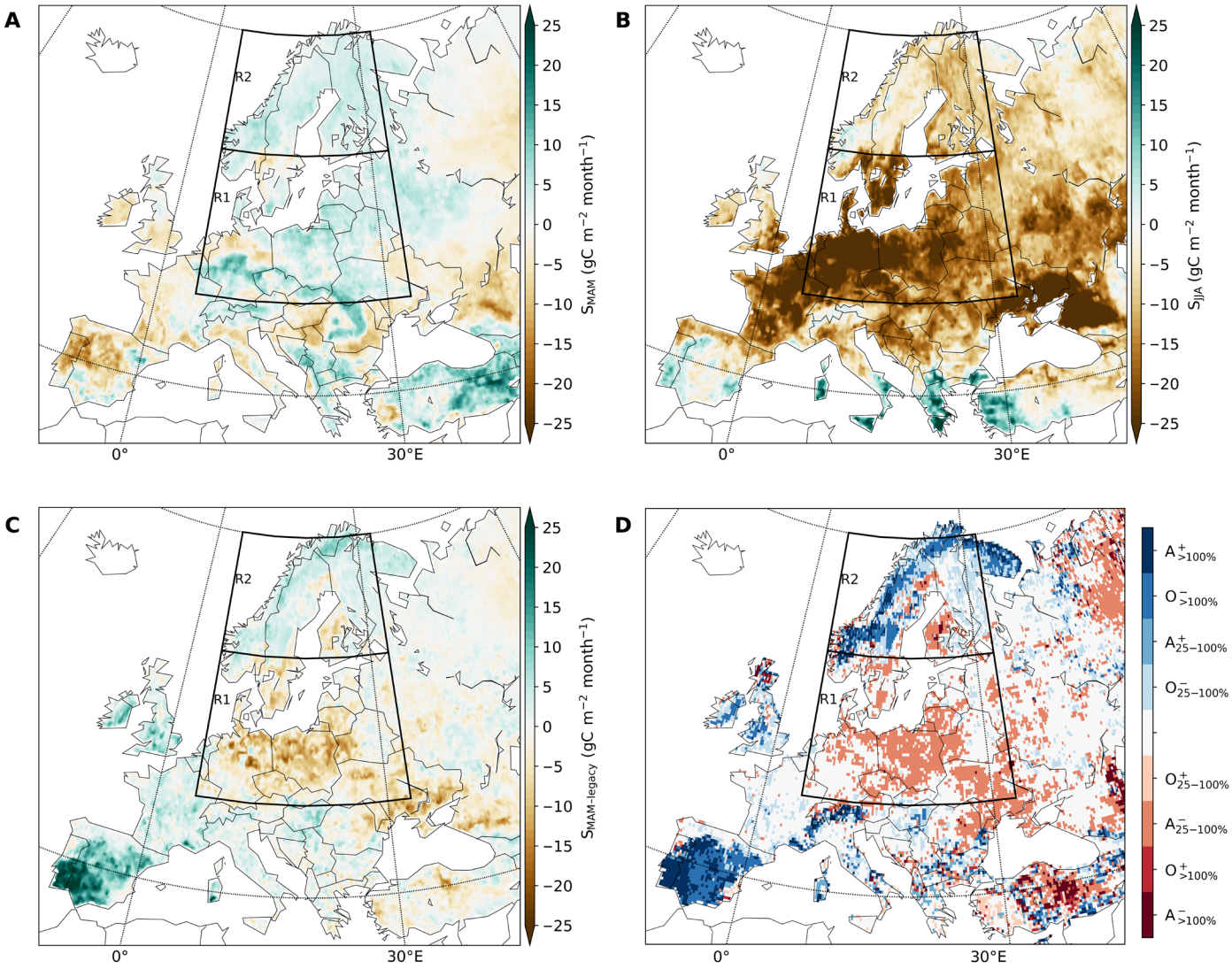

Fig. 3. Direct and legacy effects of spring and summer climate to DH2018 carbon balance. Spatial distribution of the average net effect of (**A**) spring climate anomalies direct impact on spring NBP (from S_{MAM}), (**B**) summer climate anomalies direct impact on summer NBP (from S_{JJA}), (**C**) spring climate legacy effects in JJA (from S_{MAM}), and (**D**) relative legacy impact of spring climate to summer NBP anomalies compared to the direct impact of summer climate to summer NBP anomalies. Red colors indicate regions where spring amplified (*A*) negative summer effects or offset (*O*) positive summer effects, i.e., spring contributed to a source anomaly by 25 to 100% or more than 100% of the corresponding direct summer effect. Blue colors indicate regions where spring legacy effects offset negative summer effects or amplified positive summer effects, i.e., spring legacy effects contributed to a positive summer NBP anomaly. The regions where spring legacy contributes by less than 25% of the summer-related NBP anomaly are masked in white. See the "Model simulations" section in Materials and Methods for a description of the idealized simulations used to isolate spring and summer direct and legacy effects.

climate to NBP (Fig. 3A), in spite of positive spring NBP anomalies (Fig. 2A). By contrast, DGVMs estimate a very strong direct summer-related decrease in NBP over most of Europe (Fig. 3B), including most of Scandinavia where DGVMs estimate positive summer NBP anomalies (Fig. 2A). This means that the spring conditions attenuated the direct effect of summer conditions on the loss of NBP in summer. A positive summer impact was found only in those regions where summer was wetter than average, mostly in southern Europe.

Spring legacy effects to summer NBP show regionally distinct patterns (Fig. 3C), which can be summarized in three groups: (i) regions with positive effect of spring climate on spring NBP and positive legacy NBP effects (e.g., Scandinavia, R2), (ii) regions with spring-related increase in NBP being offset by negative legacy effects (e.g., central and eastern Europe, R1), and (iii) regions with negative spring-related effects on spring NBP (weaker sink) offset by positive legacy effects (e.g., western Europe). These results reveal important differences between the spring and summer NBP anomalies (reference simulation and observations) and the individual impact of spring and summer to direct and legacy NBP anomalies (idealized simulations). While the generalized enhancement in spring CO_2 uptake might have contributed to partly offset summer carbon losses in central and western Europe, the mismatch between the NBP anomalies simulated by DGVMs for each season (Fig. 2) and those resulting from the direct impact of each individual season (Fig. 3, A and B) hints that legacy

Downloaded from http://advances.sciencemag.org/ on July 27, 2020

effects from previous seasons might compensate or offset the impact of concurrent climate anomalies during the season considered.

We thus evaluate how much spring climate legacy effects (Fig. 3C) contributed to amplify or offset the individual impact of DH2018 (Fig. 3B). In about 75% of the European area, legacy effects from spring climate contributed by 25% or more to offset or amplify the impact of DH2018 on summer NBP (Fig. 3D). In most of eastern Europe, southern Sweden, and southern Finland—the regions marked by strong spring warming and brightening—we find that spring climate anomalies contributed to amplify the negative summer impacts of DH2018 (red colors in Fig. 3D). On the contrary, higher latitude regions are dominated by positive legacy contribution of spring warming to summer NBP anomaly. In the Scandinavian mountains and parts of the Kola Peninsula, spring legacy effects offset a negative summer impact of DH2018 on summer NBP by more than 100% (values larger than 100% indicate an even stronger contribution of spring legacy than of summer direct effects to net source anomalies). In small sectors of Scandinavia (southern Norway and Kola Peninsula) as well as in the Iberian Peninsula, spring legacy effects amplified positive NBP anomalies in response to summer climate by more than 100% (i.e., doubling the sink response).

These differences cannot be solely explained by regional differences in climate conditions, as regions with similar climate anomalies (figs. S1 and S2) showed distinct contributions of different direct impacts and legacy NBP responses. As in net CO_2 uptake (Fig. 2B), a north/south asymmetry in spring legacy effects between the southern (R1) and northern (R2) sectors of DH2018 is found. We therefore analyze, in more detail, the dynamics of carbon and water fluxes in these two regions, including direct and legacy effects of spring and summer.

Regional asymmetries in net CO_2 uptake and driving processes

For R1 and R2, we evaluate the seasonal trajectories of climate anomalies (Fig. 4, A and B) and of the corresponding NBP, GPP, and TER anomalies (Fig. 4, C to G), as well as simulated SM and ET anomalies (Fig. 5, A to D). The seasonal average carbon flux anomalies for each region are summarized in Table 1.

Both regions, especially R1, started the year with weak negative (remaining above a threshold of -1σ) temperature and precipitation anomalies, and wetter than average conditions (positive $SPEI_{06}$). In R1, temperature anomalies remained above $+1\sigma$ between March and September, being the highest in April and May. While precipitation remained below average, but still within the $\pm1\sigma$ range, $SPEI_{06}$ decreased sharply concurrent with the increase in temperature and incoming radiation in March and April, remaining close to -2σ almost until the end of 2018. Region R2 shows similar evolution of climate anomalies, with precipitation being predominantly negative, but still within $\pm1\sigma$ during most of the year, and drought conditions being exacerbated with the peaks in temperature and radiation anomalies in May and July. Contrary to R1, $SPEI_{06}$ in R2 peaks in July and then recovers faster—yet remaining negative until the end of the year. The SM_{anom} simulated by DGVMs (Fig. 5) show similar evolution to that of $SPEI_{06}$ in both regions. Although relative SM_{anom} are comparable in both regions, absolute SM content peaked at lower values in R1 than in R2 (Fig. 5, A and B).

In both regions, DGVMs simulate a sharp increase in net CO_2 uptake during spring (Fig. 4, C and D), with NBP anomalies peaking in May at 15 gC m^{-2} $month^{-1}$ (40% above average) and 13 gC m^{-2} $month^{-1}$ (33% above average) in R1 and R2, respectively, and totaling over the MAM season +19 ± 26 gC m^{-2} $season^{-1}$ and +15 ± 14 gC m^{-2} $season^{-1}$ in R1 and R2, respectively. The confidence intervals correspond to the interquartile range of DGVM estimates. These net sink anomalies can be explained by a stronger increase in productivity (Fig. 4, E and F) in response to the spring warm and bright conditions than that of TER (Fig. 4, G and H). The high absolute levels of SM and strong increase in spring ET in both regions (Fig. 5) indicate a nonlimiting supply of SM in the root zone to support plant transpiration and carbon assimilation. In both R1 and R2, the peaks in spring GPP are associated with strong increase in ET, which contribute to the fast progression of drought between April and June. In the subsequent summer, autumn, and winter seasons, however, the two regions show distinct dynamics.

In region R1, the spring positive NBP anomaly was partly offset by a nonsignificant but tendentially negative summer NBP anomaly of ca. −22 ± 65 gC m^{-2} $season^{-1}$. This anomaly can be explained by enhanced summer TER (+39 ± 59 gC m^{-2} $season^{-1}$) combined with a smaller decrease of GPP anomalies to +23 ± 98 gC m^{-2} $season^{-1}$ (nonsignificant), associated with onset of water limitation (Fig. 5, A and C). Because of the persistent positive temperature anomalies, TER remained above average until the end of the year, while GPP recovered in September and October, decreasing again until December. As a result, the MMEM indicates a small positive NBP anomaly during September to November, followed by a weak negative NBP anomaly in December. Over the full year 2018, R1 was neutral, with an annual NBP anomaly of −8 ± 80 gC m^{-2} $year^{-1}$, although DGVMs show a wide range of estimates.

In region R2, DGVMs estimate above-average productivity and respiration over most of the year, with seasonal dynamics following that of temperature anomalies. Over spring and summer, the significant positive anomalies in GPP (+28 ± 16 gC m^{-2} $season^{-1}$ and +48 ± 22 gC m^{-2} $season^{-1}$; Table 1 and Fig. 4D) are stronger than the increase in TER (+15 ± 13 gC m^{-2} $season^{-1}$ and +35 ± 22 gC m^{-2} $season^{-1}$; Fig. 4F) and result in increased NBP in both seasons, although not significant in summer given the ensemble uncertainty (Table 1 and Fig. 4B). The persistence of higher than average GPP in R2 appears to be supported by higher absolute levels of SM and sufficient supply for transpiration (Fig. 5, B and D). Because DGVMs estimate a stronger anomaly in TER than in GPP and a small source anomaly from August onward, their annual balance was close to neutral (ca. +10 ± 63 gC m^{-2} $year^{-1}$), as for R1.

Regional asymmetries in seasonal direct and legacy effects

The regionally integrated individual effects of spring and summer climate on NBP, GPP, and TER anomalies based on the attribution simulations are shown in Fig. 4 (C to H) as blue and red lines for SMAM and SJJA, respectively.

Direct and legacy spring effects

As shown in Fig. 4 (C and D) and summarized in Table 1, the MMEM estimates a positive spring effect on NBP (increased uptake) in both regions, but in R1, spring climate contributes only to a small fraction of the positive spring NBP anomaly (compare blue and black lines). In both regions, the DGVMs attribute the positive spring contribution to NBP to an increase in productivity (+29 ± 23 and +30 ± 14 gC m^{-2} $season^{-1}$, in R1 and R2, respectively) in response to spring warming and brightening. In R2, the positive direct effect of spring on GPP is stronger than the corresponding increase in TER due to warming (+18 ± 10 gC m^{-2} $season^{-1}$; Table 1), while in R1,

Downloaded from http://advances.sciencemag.org/ on July 27, 2020

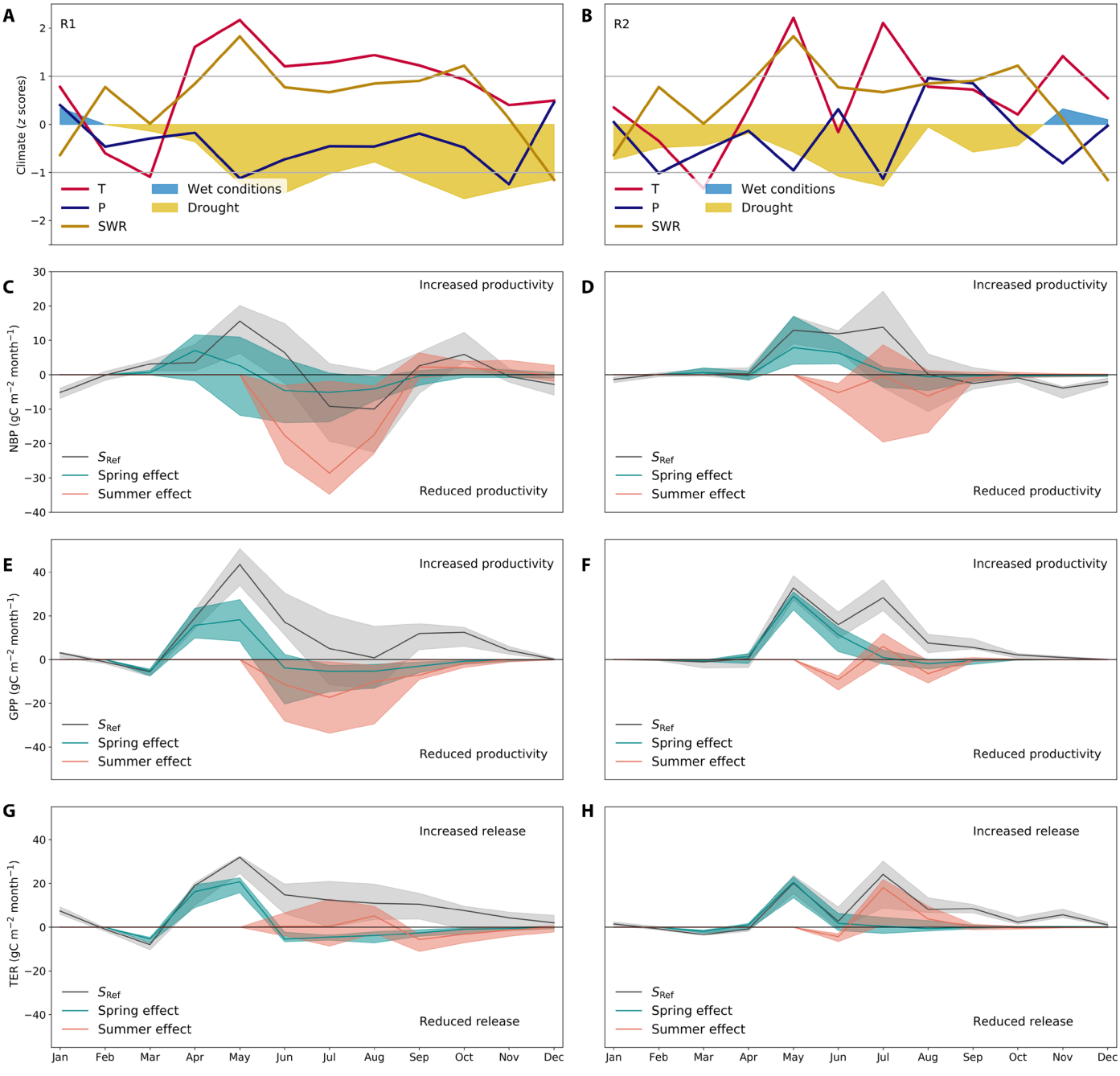

Fig. 4. Seasonal evolution of climate and net CO_2 uptake during 2018 in the two study regions. Spatially averaged standardized anomalies in monthly mean temperature (T, red lines), precipitation (P, blue lines), incoming solar shortwave radiation (SWR, yellow lines), and $SPEI_{06}$ (shaded areas, blue for wetter-than-average conditions, yellow for drier-than-average conditions) for R1 (**A**) and R2 (**B**), respectively. The horizontal lines delimit the ±1 SD interval of the 1979–2018 period. In (**C**) and (**D**), the corresponding regional anomalies in NBP (back line and gray shades for MMEM and model interquartile range, respectively) estimated by the ensemble of 11 DGVMs for R1 and R2, respectively. Note the different *y*-axis range in (C) and (D). The blue (red) line indicates the individual effect of spring (summer) climate, and the interquartile range is shown by the shaded area. These effects are estimated by the factorial simulations with climatological spring (summer), i.e., S_{MAM} (S_{JJA}), as described in Materials and Methods. As in (C) and (D), (**E**) and (**F**) show the corresponding 2018 GPP anomalies, and (**G**) and (**H**) show the TER anomalies in 2018 for both regions. The annual totals of flux anomalies, as well as the contribution of spring and summer climate anomalies to the annual balance, are given in Table 1.

the TER increase is comparable to that of GPP (+30 ± 12 gC m^{-2} $season^{-1}$). The two regions further differ in their spring legacy effects on summer and autumn fluxes.

In region R1, the DGVMs estimate stronger spring GPP and TER anomalies than those solely explained by spring climate alone, suggesting that the legacy effects from winter of 2018 or long-term trends also contributed to high spring GPP and TER. The spring-related increase in spring GPP is cancelled out by a negative legacy effect of spring climate to summer GPP (−34 ± 54 gC m^{-2} $season^{-1}$; Fig. 4E). This negative legacy of spring warming to summer GPP can be

Downloaded from http://advances.sciencemag.org/ on July 27, 2020

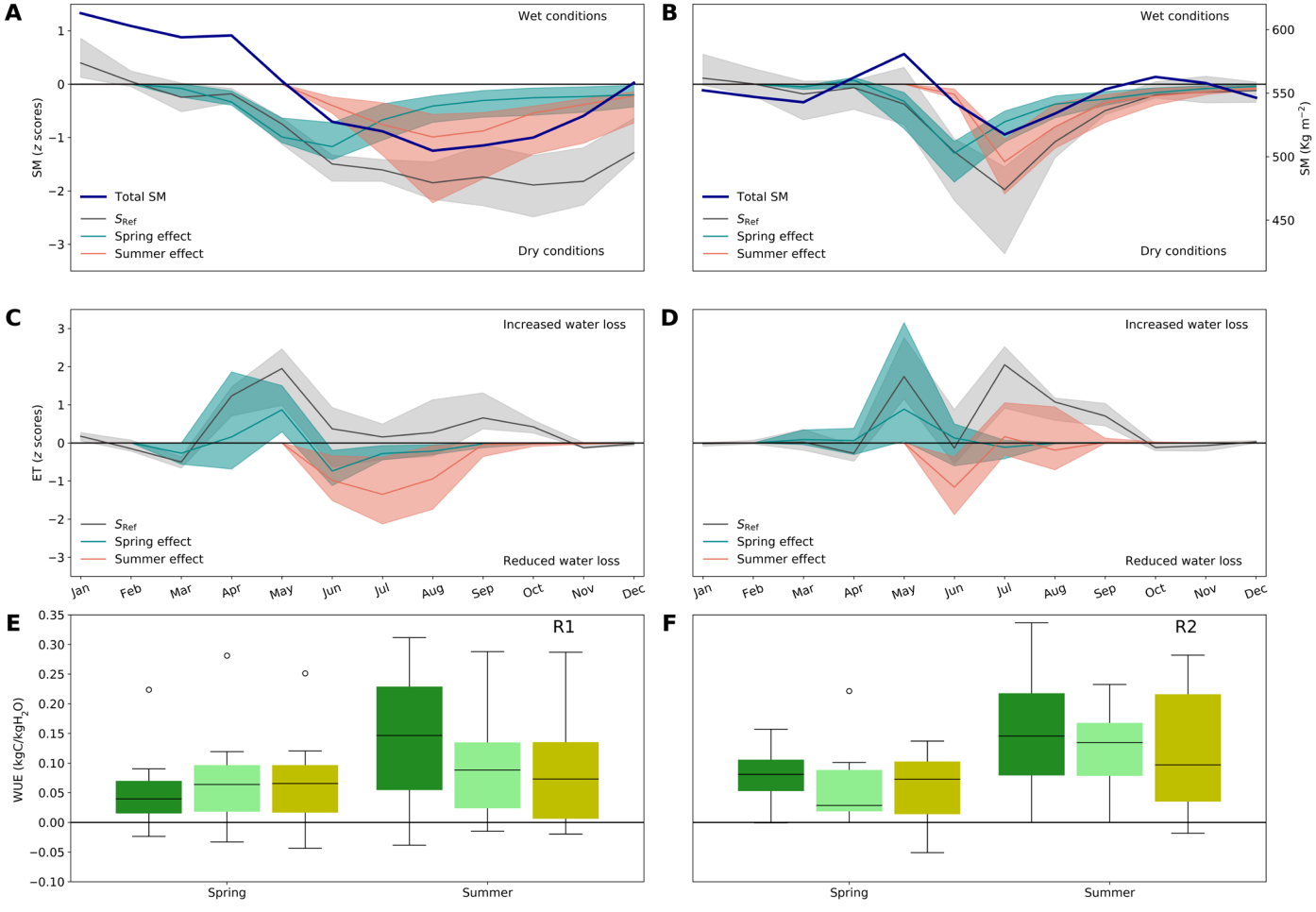

Fig. 5. Seasonal evolution of hydrological variables during 2018 in the two study regions. Standardized anomalies in total SM from the MMEM of the reference simulation (black line) and its uncertainty (shaded gray area) in R1 (**A**) and R2 (**B**). The blue (red) line indicates the individual effect of spring (summer) climate, and the interquartile range is shown by the shaded area. Absolute regional average SM values (in kg m^{-2}) are given by the blue lines. The corresponding anomalies in ET are shown in (**C**) and (**D**) for R1 and R2, respectively. The distribution of the anomalies in WUE (defined as GPP/ET) estimated by the DGVM ensemble for forests (dark green), grasslands (light green), and croplands (yellow) in R1 (**E**) and R2 (**F**) during spring and summer 2018. WUE per land-cover type was calculated by weighting pixel-scale WUE by the corresponding pixel land-cover fraction of forests, grasslands, and croplands. It should be noted that these values will still include mixed signals from the three vegetation classes, especially in R1 where land-cover composition per pixel is more mixed.

Downloaded from http://advances.sciencemag.org/ on July 27, 2020

explained by an SM deficit legacy promoted by increased spring ET (Fig. 5C) that contributed to the quick onset of drought and explained 47% of the average summer SM_{anom} (Fig. 5A) and led to reduced GPP in summer (Fig. 4). The DGVMs also estimate a negative spring legacy to summer TER (−14 ± 12gC m^{-2} season^{-1}; Fig. 4G). This reduction, though, is smaller than the reduction in productivity, therefore resulting in a negative spring legacy effect to summer NBP (Fig. 4C). Such a negative legacy of spring climate to GPP and TER not only prevails during summer but also extends until the following winter, being progressively attenuated as spring legacy SM deficits slowly attenuate. This results in a weakly negative contribution of spring climate to the annual NBP of ca. −10 ± 49 gC m^{-2} in R1 (Table 1).

In region R2, most of the anomalies in spring carbon fluxes can be explained by spring climate conditions, that is, no legacy effect of previous winter conditions on carbon fluxes (Fig. 4, D, F, and H, and Table 1). As in R1, increased spring ET promotes a quick progression of drought conditions and strong drought during summer for R2, with the spring legacy explaining 57% of the summer SM_{anom} (Fig. 5B). However, the spring-related legacy effects on summer GPP are much smaller than in R1 (+10 ± 15 gC m^{-2} season^{-1}; Table 1) as well as on GPP in subsequent seasons (Fig. 4F), possibly because of still sufficient absolute water supply to support productivity (Fig. 5B). Therefore, the individual effect of spring in the annual NBP anomaly of region R2 results only in a weak positive annual NBP anomaly of +7 ± 30 gC m^{-2}, in contrast with R1.

Summer effects

Summer climate imposed concurrent negative NBP anomalies (Fig. 4, C and D, red lines) in both regions, but much stronger in R1 (−72 ± 82 gC m^{-2} season^{-1}) compared to R2 (−15 ± 30 gC m^{-2} season^{-1}).

In region R1, the summer-related negative NBP anomaly can be explained by a strong reduction of summer GPP in response to drought despite a weak TER enhancement (−44 ± 81 and +3 ± 43 gC m^{-2} season^{-1}, respectively; Table 1). The summer legacy anomalies in both GPP

Table 1. Direct and legacy anomalies in regional carbon fluxes. Annual, spring, and summer integrated anomalies in NBP, GPP, and TER from the baseline simulation (S_{Ref}) and the corresponding individual contributions of spring and summer climate, estimated by the two idealized simulations (S_{MAM} and S_{JJA}). The anomaly values correspond to the MMEM, and the uncertainty is given by the interquartile range of the 11 DGVMs. The asterisks indicate ensemble anomalies significantly different than zero at 95% (*) and 99% (**) confidence levels estimated by a two-tailed Wilcoxon's signed-rank test on the seasonal anomalies of the 11 DGVMs. Units: gC m^{-2} season^{-1} for spring and summer values, and gC m^{-2} year^{-1} for annual values.

Anomaly		R1			R2		
		S_{Ref}	Spring effect	Summer effect	S_{Ref}	Spring effect	Summer effect
NBP	Annual	−8 ± 80	−10 ± 49	−63 ± 91	10 ± 63	7 ± 30	−24 ± 26
	Spring (MAM)	19 ± 26*	5 ± 29	–	15 ± 14*	8 ± 15*	–
	Summer (JJA)	−22 ± 65	−22 ± 42	−72 ± 82*	15 ± 49	7 ± 9	−15 ± 30
GPP	Annual	89 ± 116*	−2 ± 28	−44 ± 97	89 ± 30 **	35 ± 14 **	−10 ± 29
	Spring (MAM)	56 ± 19**	29 ± 23	–	28 ± 16 **	30 ± 14 **	–
	Summer (JJA)	23 ± 98	−30 ± 54*	−44 ± 81	48 ± 22 **	10 ± 15	−10 ± 29
TER	Annual	90 ± 88 **	14 ± 34	−12 ± 42	71 ± 31 **	21 ± 20 **	12 ± 19
	Spring (MAM)	37 ± 17 **	30 ± 12 **	–	15 ± 13 **	18 ± 10 **	–
	Summer (JJA)	39 ± 59*	−14 ± 12*	3 ± 43	35 ± 22 **	3 ± 15	15 ± 21

and TER last until the end of the year, being progressively attenuated as legacy summer SM deficits become weaker (Fig. 5). The decrease in TER as legacy from summer climate is slightly stronger than that of GPP during autumn, explaining a very weakly positive NBP anomaly summer legacy between September and November. The annual NBP anomaly from summer effects in R1 is thus −63 ± 91 gC m^{-2}, six times stronger than the spring effects.

In region R2, summer-related NBP anomalies can be explained by GPP decrease and concurrent TER increase (Table 1), but with variable intraseasonal dynamics. Negative impact on summer NBP is due to both decreased GPP in June and August and to increased TER in July and August (Fig. 4, D, F, and H). The sharp drop in summer-related GPP, TER, and NBP anomalies in June coincides with close to average temperatures, and wetter and brighter than average conditions (Fig. 4B). DGVMs also estimate a positive contribution of warming (Fig. 4B) in July to GPP, despite prevailing SM deficits, possibly as a result of a slight increase in rainfall and decreased ET in June (Figs. 4B and 5).

DISCUSSION

Spring warming and the onset of summer drought in 2018

In contrast to the drought-heat events in 2003 and 2010 in Europe, DH2018 was particular in that it showed the fastest transition from relatively wet conditions in winter to severe drought in summer. The extreme spring warming and brightening is also a distinctive feature of 2018.

Using an ensemble of DGVMs, we found that the warm and bright conditions in spring 2018 led to an increase in vegetation productivity and net CO_2 uptake (Figs. 2 to 4), by advancing the growing season onset and stimulating spring photosynthesis. However, increased spring vegetation productivity contributed to increased ET, leading to the fast depletion of SM in late spring and summer (Fig. 5). While in DH2003 and DH2010, the summer drought was collocated with extreme summer warming (*14*), that is only the case for the southern sector of the DH2018 affected area (Fig. 1 and fig. S1). The results from simulation S_{MAM} show that, in the regions affected by DH2018, the legacy effects from increased ET in spring contributed by about as much as the adverse summer climate conditions to the summer drought (Fig. 5). At the European scale, and especially in the DH2018 region, the SM deficits in summer from spring legacy match better the anomalies in spring GPP and ET (fig. S6) than the corresponding spring/summer temperature anomalies, indicating a relevant contribution of spring vegetation water use to the amplification of DH2018. Previous studies have discussed the importance of preceding warm and dry springs to the onset of DH2003 and DH2010 (*6*, *14*). The regions affected by these two events also registered sunnier than average conditions in spring (fig. S2), which likely stimulated GPP and ET, as shown in this study for DH2018. Therefore, information about vegetation activity in spring could be used as an additional early warning indicator for extreme summers, and potentially used for seasonal or subseasonal predictability.

Regional asymmetries

In the previous extreme summers of 2003 and 2010, most, if not all, of the areas affected by drought and heat during summer registered strong reductions in productivity and net CO_2 uptake (*2*, *7*, *10*). Flach *et al.* (*9*), though, pointed out to some exceptions in the higher-latitude regions during DH2010, where increased GPP was estimated during summer, because extreme warming approached photosynthesis optimal temperatures. For DH2018, we found a similar increased summer productivity and net CO_2 uptake in most of Scandinavia (R2) and the opposite in the southern sectors of DH2018 (R1). The DGVM MMEM results are supported by observation-based datasets (Fig. 2 and figs. S3 to S5) as well as satellite-based leaf area index from Albergel *et al.* (*17*). In Scandinavia, daily mean and maximum temperatures during summer were, on a seasonal average, close to but below 25°C, including the regions with record-breaking warming, in contrast with much of central Europe that registered daily maximum temperatures above 25°C over JJA (fig. S7).

The asymmetry in summer NBP anomalies between R1 and R2, though, cannot be solely explained by distinct responses of ecosystems to DH2018, as the simulations designed to isolate the effect of summer show a negative impact of the extreme summer drought on GPP

Downloaded from http://advances.sciencemag.org/ on July 27, 2020

and NBP in both regions (Figs. 3 and 4 and fig. S6). These results are in line with previous studies reporting systematically negative effects of summer drought and heat on vegetation productivity (*2*, *7*, *10*). By isolating the spring and summer impacts on ecosystem activity, we found that asymmetries in summer NBP and GPP anomalies can be explained by distinct legacy effects of increased spring vegetation growth to summer productivity between R1 and R2 (Figs. 3D and 4).

In the northern sector of DH2018 (most of R2), spring legacy effects offset, in part or completely, the carbon losses due to summer heat and drought (Fig. 3D). In western Scandinavia and Northern Russia, enhanced spring productivity contributed to an increased carbon sink in subsequent months through increased leaf growth, which helped to sustain higher photosynthesis levels over summer and offset the negative impact of DH2018 (Figs. 3D and 4 and fig. S6). It is likely that 2010 spring legacy effects explain the positive summer GPP anomalies in northern areas affected by DH2010 pointed out by Flach *et al.* (*9*), because these regions had also experienced extreme spring warming in 2010. However, more biomass also requires more energy to maintain over summer, resulting in an increase in autotrophic respiration (fig. S6), increased buildup of fuel for summer fires (fig. S4), and increased litterfall, providing more substrate for decomposition over late summer to winter. This results in a weak spring contribution to the annual NBP in R2 (Fig. 4). The intraseasonal dynamics of carbon and water fluxes in R2 indicates a prevailing temperature-limited regime, which indicates that although drought in R2 was comparable, in relative terms, to R1, the higher absolute SM content in R2 during summer (Fig. 5) was enough to support vegetation productivity. On the contrary, in the southern areas of DH2018 (R1), as well as in the Baltic sector of R2, earlier and stronger spring growth and ET in 2018 led to an exceptionally fast onset of drought (Fig. 5) and to subsequent plant collapse (Fig. 4), as the additional biomass produced in spring suddenly became more difficult to sustain underwater stress. The spring-related decrease in GPP in R1 during summer suggests strong summer water limitation.

The distinct seasonal compensation effects between the northern and southern regions can, thus, be partly explained by different limitation regimes: the mountainous and northern sectors of R2 maintaining a temperature-limited regime, and R1 and the southern Baltic coastal areas of R2 transitioning to a summer water-limited regime. A small band along the western coast of Scandinavia had positive rainfall anomalies in summer (fig. S1) and less extreme SM deficits (Fig. 1), which might have provided enough water supply to support increased GPP and ET over summer. Nevertheless, we find positive spring legacy effects in some regions with strong summer drought and rainfall deficits. Therefore, we evaluate whether differences in land-cover type and WUE can explain the different limitation regimes in R1 and R2 (Fig. 5).

Consistent with (*9*, *11*), we find that those areas within the DH2018 region where spring contributed positively to summer NBP were dominated by forests (fig. S8), while the regions where spring had negative effects on summer CO_2 uptake were associated with higher cropland fractions. On the one hand, trees have deep roots and can access deep water reserves, while crops and grasses cannot. In addition, trees are better able to regulate stomatal conductance and increase WUE under drought stress (*8*, *12*), attenuating early water loss from increased spring warming and enhanced productivity. Most ecosystems in R2 are forests, with only the southern Baltic sectors of R2 having a higher fraction of croplands, and R1 is largely dominated by agricultural areas. DGVMs simulate higher WUE rates in summer over pixels dominated by forests and grasslands than those dominated by croplands, consistent with observation-based studies (*11*), and an increase in WUE during the summer drought (*8*) in both regions (Fig. 5). However, the two regions also differ in spring, with WUE in R1 being lower for forests and croplands compared to R2. This implies that in R1, increased vegetation growth during spring happened at a higher cost of water, amplifying summer SM deficits and shifting the ecosystems into a water-limited regime. The stronger spring SM depletion in R1 compared to R2 might, in turn, have contributed to the higher summer temperature anomalies registered in the southern sector of DH2018 from increased sensible heat fluxes (fig. S1).

Model experiments and evaluation

Our results show that the impact of a given extreme event on ecosystems cannot be quantified by simply evaluating co-occurring anomalies in carbon fluxes, because these are—at least partly—history dependent. Likewise, legacy effects cannot be isolated by comparing anomalies in carbon fluxes between seasons, because they include carry-on effects from other seasons in addition to the anomalies due to the concurrent climate anomalies, and interseasonal correlation between climate anomalies is generally low. Quantifying the individual contribution of a given climate extreme to the net seasonal and annual carbon balance thus requires model experiments designed to isolate these effects.

Using an ensemble of 11 DGVMs with idealized simulations to attribute CO_2 flux anomalies to the individual impacts of spring (S_{MAM}) and summer (S_{JJA}) abnormal climate conditions, we found more widespread positive and negative legacy effects from warm spring to summer carbon fluxes during DH2018 than shown by Buermann *et al.* (*15*). In their study, Buermann *et al.* (*15*) used global simulations at coarser spatial and temporal resolution and considered the whole period 1982–2011 by comparing differences between summer and spring anomalies over multiple years, in which warm springs are not always necessarily followed by warm/dry summer conditions. Here, we focus on an extreme isolated event and our results are based on factorial runs designed to specifically attribute direct concurrent and legacy effects of spring (and summer) conditions to carbon flux anomalies. Our results are, thus, valid only for the specific case of the extreme spring and summer of 2018, in which the legacy signal is probably stronger than in other years.

We assess the effects of aggregated spring climate anomalies in 2018 on carbon and water fluxes. These anomalies include slightly below-average rainfall and increased spring radiation. Because warming/brightening and drying are coupled through surface feedbacks (*14*), identifying the individual contribution of spring warming versus spring rainfall and radiation, or the individual role of vegetation in amplifying or dampening summer climate anomalies would require specific simulations or the analysis of multiple events with different anomaly combinations. Nevertheless, the method proposed here to quantify the individual contribution of a given climate anomaly could be applied on single climate variables to isolate their individual effect. The method could further be extended to other events and used to evaluate legacy effects from other seasons (e.g., winter), providing a more comprehensive understanding on seasonal compensation effects in the carbon cycle.

We have found that the MMEM of key variables simulated by DGVMs generally matches well several observation-based datasets. Both the spatial patterns and seasonal dynamics of drought was

Downloaded from http://advances.sciencemag.org/ on July 27, 2020

shown to be well captured by the DGVM MMEM compared to both SM from ERA5 and surface SM from satellite microwave measurements (figs. S4 and S6). Likewise, the DGVM MMEM also shows good agreement in the spatial patterns of summer 2018 GPP anomalies compared to the FLUXCOM data-driven product based on eddy covariance measurements and of simulated aboveground biomass changes with vegetation optical depth from satellite microwave observations (figs. S4 and S5). Schewe *et al.* (*3*) analyzed simulations from global vegetation models (some of them used in this study) and concluded that models underestimated the impacts of extreme events on ecosystems. We find that the DGVM MMEM locates extremes in GPP consistent with FLUXCOM, especially during summer. A possible reason for the better agreement of the simulations in this study with observations compared to global runs of the same models is the use of the new ERA5 forcing, which has improved performance in Europe (*18*), and increased temporal and spatial resolution compared to previous global DGVM simulations, which should better represent spatial and temporal extremes in climate variables.

Despite the good agreement between DGVM MMEM and observation-based datasets, there is still a large dispersion among models in the strength (and in a few cases, the sign) of the flux anomalies (Fig. 4, Table 1, and fig. S9). The good skill of the MMEM in spite of the wide model range in modeled carbon fluxes in response to climate anomalies is not particular to our study. For example, Bastos *et al.* (*19*) have shown the improved performance of the ensemble mean of 16 DGVMs (relative to that of individual models) in capturing the response of tropical ecosystems to El Niño warming and drying, compared with atmospheric data and satellite observations. We find that models differ more (i.e., have a wider between-model range) in their estimates of the absolute anomalies in spring and summer 2018 than in the individual contribution of spring and summer climate anomalies to carbon fluxes (Table 1). Although the individual impacts of each season cannot be validated with observations, this increases confidence in our findings about seasonal direct and legacy effects. Nevertheless, our results highlight the need for caution when quantifying climate impacts using individual models.

Last, extreme events and the response of ecosystems are expected to be modulated by local conditions, for examples, local soil depth and texture or tree species composition, which cannot be captured by these large-scale simulations. We also note that DGVMs do not simulate wetlands and peatlands that usually keep high water tables. Rooting depth in DGVMs is also highly variable, and root water uptake processes are usually oversimplified (*20*). To understand how these limitations affect DGVM estimates, results can be evaluated by direct site-scale simulations and direct comparison with eddy covariance data.

CONCLUSIONS

In summer 2018, Europe registered the largest extent affected by extreme drought when compared with previous extreme summers of 2003 and 2010 (DH2003 and DH2010). However, not all areas under extreme drought were associated with extreme summer heat or precipitation deficits. The 2018 extreme summer drought and heat event differed from DH2003 and DH2010 by (i) its geographical distribution, centered in higher-latitude regions; (ii) a sudden transition from wet spring to dry summer conditions; and (iii) a strong preceding heat wave in spring.

We found strong regional asymmetries with different sign of the carbon flux anomalies during extreme drought between central/eastern Europe (reduced CO_2 uptake) and Scandinavian (increased CO_2 uptake) ecosystems, supported by observation-based datasets. Using process-based models, we show that DH2018 affected negatively ecosystems' CO_2 uptake, consistent with previous findings for DH2003 and DH2010. The asymmetries in summer CO_2 uptake were rather explained by distinct legacy effects of spring warming and brightening to the summer SM deficits and carbon cycle fluxes, partly mediated by distinct vegetation responses to progressive drying. Our results thus support a negative direct impact of extreme summer drought and heat on ecosystems, expected to increase in frequency or intensity in the future. Whether these summer carbon losses might be compensated by a comparable increase in favorable spring conditions depends on the evolution of seasonal climate patterns.

Moreover, our results stress the importance of spring climate conditions and of ecosystem dynamics in amplifying or dampening the summer carbon and water anomalies, which can potentially be useful to predict summer extremes in advance. The important role of land cover in mediating the seasonal legacy effects and attenuating/amplifying impacts of summer drought suggests a potential role of future land-management strategies under increasing temperature to influence patterns of summer heat waves and droughts. Future modeling experiments evaluating the role of vegetation cover in mediating the development of drought-heat extremes are needed.

MATERIALS AND METHODS

Climate fields

Here, we use the most recent atmospheric reanalysis from the European Center for Medium-Range Weather Forecast (ECMWF), the ERA5 Reanalysis, which provides climate fields at 0.25° spatial and hourly temporal resolution from 1979 until present. ERA5 has several improved features compared to the ERA-Interim product, particularly finer spatial and temporal resolution, which allow better representation of extremes, and improved performance over Europe relative to other datasets, particularly SM (*18*). Although SM is not used as forcing for our model simulations, the better performance of ERA5 is indicative of improved hydrology.

Drought conditions

To assess agricultural drought conditions, we use the volumetric soil water content fields from ERA5 (0 to 289 cm). To compare between regions and with simulated SM from DGVMs, which have variable soil depth, we analyze standardized anomalies (*z*-score units). These are calculated by removing the average seasonal cycle and dividing by the long-term SD on a pixel basis. Extreme drought was defined as values of SM_{anom} below −2.5 SD units, and severe drought was defined as values of SM_{anom} between −2.5 and − 2 SD units. The extent affected by extreme and severe drought was calculated by summing up the area corresponding to the pixels within each drought class. Extreme and severe droughts are, however, dependent on how drought is calculated. We therefore further estimate drought conditions by analyzing the probability distribution of SM for each pixel, as proposed by Sheffield *et al.* (*21*). We first evaluate the probability distribution that provides the best fit for the pixel's summer SM_{anom} over the 40 years (evaluated by the Kolmogorov-Smirnov test) and then calculate the cumulative probability of a given SM_{anom}.

Downloaded from http://advances.sciencemag.org/ on July 27, 2020

FLUXCOM

FLUXCOM uses carbon and energy fluxes and meteorological measurements at site-level, gridded spatial-temporal information from remote sensing (RS) and meteorological datasets (Meteo) together with machine learning (ML) techniques to scale up these fluxes to global extents (*16*, *22*). The purely data-driven estimates are independent to process-based DGVM model output. Here, we use the ensemble estimate of GPP from three ML methods together with two flux partitioning methods (RS + Meteo) driven by daily ERA5 meteorological forcing for the period 1979–2018. The FLUXCOM product is known to underestimate the magnitude of interannual variability (*22*). Therefore, we show results of GPP and TER anomalies as standardized anomalies.

Above-ground biomass and SM from L-VOD

The SMOS-IC SM and L-VOD data were retrieved from a two-parameter inversion of the L-MEB model (L-band microwave emission of the biosphere) from the multiangular and dual-polarized SMOS observations between 2010 and 2018 (*23*). We used the SMOS SM and L-VOD product in the IC version (*24*).

We used the 30 "best" observations from the combined observations acquired from the ascending and descending orbits. Best observations were selected based on the criteria of lowest values of the TB-RMSE (brightness temperature – root mean square error) index, an index used to evaluate the impact of radio-frequency interference (RFI) effects (*24*). All observations were initially filtered by considering the condition TB-RMSE $\leq$ 8K to ensure low overall RFI effects.

The annual median of the L-VOD index has been found to be a good proxy of above-ground biomass (*25*). The SMOS-IC product has been found to be very accurate in several intercomparison studies of microwave remotely sensed L-VOD and SM retrievals.

Model simulations

To evaluate the response of ecosystems to the climate anomalies, we used 11 DGVMs: CABLE-POP (*26*), ISBA-CTRIP (*27*), DLEM (*28*), ISAM (*29*), JSBACH (*30*), LPJ-GUESS (*31*), LPX (*32*), OCN (*33*), ORCHIDEE (*34*), ORCHIDEE-MICT (*35*, *36*), and SDGVM (*37*). Three factorial simulations were run for the European domain between 32°N and 75°N and −11°E and 65°E, following a spin-up to equilibrate carbon pools.

In simulation S_{Ref}, the models were forced with observed annual CO_2 concentration and changing climate between 1979 and 2018 and fixed land-cover map from 2010 (table S1). The CO_2 concentration values were obtained from (*38*); the climate fields were the hourly fields from ERA5 reanalysis dataset described above; and the land-cover map was obtained from the LUH2v2h dataset (*39*). The effects of land-use change were not considered because they should not contribute significantly to annual anomalies, and our focus is the effect of climate extremes on ecosystem dynamics. For those models including nitrogen cycling, nitrogen forcing from the N_2O Model Inter-Comparison Project (NMIP) project was used (*40*).

Two additional simulations for 2018 were run in which the DGVMs were forced with the 2018 fields from ERA5 in all months except spring (MAM; simulation S_{MAM}) and summer (JJA; simulation S_{JJA}), which were forced with climatological values (average hourly fields for 1979–2018) as described in table S1. The difference between the baseline simulation (S_{Ref}) and S_{MAM} (S_{JJA}) provides the individual contribution of spring (summer) climate to the anomalies in the concurrent season (i.e., the direct effects of MAM or JJA climate anomalies on surface energy, water, and carbon exchanges) and in the subsequent seasons. Because the simulations S_{MAM} and S_{JJA} are run until the end of 2018 with the same climate forcing as S_{Ref}, the differences in the simulated surface exchanges in the subsequent seasons can only be due to legacy effects on SM from the climate anomalies in spring (S_{MAM}) or summer (S_{JJA}) combined with the response of ecosystems to those anomalies.

Because models show a wide range of anomaly responses to droughts and a few models stand out as outliers, we use MMEM, instead of a simple mean, for the ensemble estimates. The weights were based on the model's correlation of the European-scale spatial and temporal variability of GPP between March and August with that of FLUXCOM.

Water-use efficiency was defined as WUE = GPP/ET, because not all models output transpiration separately. Likewise, not all models output GPP and ET per plant functional type individually. Therefore, to estimate WUE in the two study regions for different land-cover types, pixel-level WUE was weighted by the corresponding land-cover fraction of forests, grasslands, and croplands in LUH2v2h, but it should be noted that these values will still include mixed signals from the three vegetation classes.

SUPPLEMENTARY MATERIALS

Supplementary material for this article is available at http://advances.sciencemag.org/cgi/content/full/6/24/eaba2724/DC1

REFERENCES AND NOTES

1. D. Barriopedro, E. M. Fischer, J. Luterbacher, R. M. Trigo, R. García-Herrera, The hot summer of 2010: Redrawing the temperature record map of Europe. *Science* **332**, 220–224 (2011).
2. P. Ciais, M. Reichstein, N. Viovy, A. Granier, J. Ogée, V. Allard, M. Aubinet, N. Buchmann, C. Bernhofer, A. Carrara, F. Chevallier, N. De Noblet, A. D. Friend, P. Friedlingstein, T. Grünwald, B. Heinesch, P. Keronen, A. Knohl, G. Krinner, D. Loustau, G. Manca, G. Matteucci, F. Miglietta, J. M. Ourcival, D. Papale, K. Pilegaard, S. Rambal, G. Seufert, J. F. Soussana, M. J. Sanz, E. D. Schulze, T. Vesala, R. Valentini, Europe-wide reduction in primary productivity caused by the heat and drought in 2003. *Nature* **437**, 529–533 (2005).
3. J. Schewe, S. N. Gosling, C. Reyer, F. Zhao, P. Ciais, J. Elliott, L. Francois, V. Huber, H. K. Lotze, S. I. Seneviratne, M. T. H. van Vliet, R. Vautard, Y. Wada, L. Breuer, M. Büchner, D. A. Carozza, J. Chang, M. Coll, D. Deryng, A. de Wit, T. D. Eddy, C. Folberth, K. Frieler, A. D. Friend, D. Gerten, L. Gudmundsson, N. Hanasaki, A. Ito, N. Khabarov, H. Kim, P. Lawrence, C. Morfopoulos, C. Müller, H. Müller Schmied, R. Orth, S. Ostberg, Y. Pokhrel, T. A. M. Pugh, G. Sakurai, Y. Satoh, E. Schmid, T. Stacke, J. Steenbeek, J. Steinkamp, Q. Tang, H. Tian, D. P. Tittensor, J. Volkholz, X. Wang, L. Warszawski, State-of-the-art global models underestimate impacts from climate extremes. *Nat. Commun.* **10**, 1005 (2019).
4. D. Barriopedro, P. M. Sousa, R. M. Trigo, R. García-Herrera, A. M. Ramos, The exceptional Iberian heatwave of summer 2018. *B. Am. Meteorol. Soc.* **101**, S29–S34 (2020).
5. V. D'Agostino, Drought in Europe Summer 2018: Crisis management in an orderly chaos; https://www.farm-europe.eu/blog-en/drought-in-europe-summer-2018-crisis-management-in-an-orderly-chaos/ [cited 2019 October 14].
6. E. M. Fischer, S. I. Seneviratne, D. Lüthi, C. Schär, Contribution of land-atmosphere coupling to recent European summer heat waves. *Geophys. Res. Lett.* **34**, L06707 (2007).
7. M. Reichstein, P. Ciais, D. Papale, R. Valentini, S. Running, N. Viovy, W. Cramer, A. Granier, J. Ogée, V. Allard, M. Aubinet, C. Bernhofer, N. Buchmann, A. Carrara, T. Grünwald, M. Heimann, B. Heinesch, A. Knohl, W. Kutsch, D. Loustau, G. Manca, G. Matteucci, F. Miglietta, J. M. Ourcival, K. Pilegaard, J. Pumpanen, S. Rambal, S. Schaphoff, G. Seufert, J.-F. Soussana, M.-J. Sanz, T. Vesala, M. Zhao, Reduction of ecosystem productivity and respiration during the European summer 2003 climate anomaly: A joint flux tower, remote sensing and modelling analysis. *Glob. Chang. Biol.* **13**, 634–651 (2007).
8. W. Peters, I. R. van der Velde, E. Van Schaik, J. B. Miller, P. Ciais, H. F. Duarte, T. van der Laan-Luijkx, M. K. van der Molen, M. Scholze, K. Schaefer, P. L. Vidale, A. Verhoef, D. Wårlind, D. Zhu, P. P. Tans, B. Vaughn, J. W. C. White, Increased water-use efficiency and reduced CO_2 uptake by plants during droughts at a continental scale. *Nat. Geosci.* **11**, 744–748 (2018).

Downloaded from http://advances.sciencemag.org/ on July 27, 2020

9. M. Flach, S. Sippel, F. Gans, A. Bastos, A. Brenning, M. Reichstein, M. D. Mahecha, Contrasting biosphere responses to hydrometeorological extremes: Revisiting the 2010 western Russian heatwave. *Biogeosciences* **16**, 6067–6085 (2018).
10. A. Bastos, C. M. Gouveia, R. M. Trigo, S. W. Running, Analysing the spatio-temporal impacts of the 2003 and 2010 extreme heatwaves on plant productivity in Europe. *Biogeosciences* **11**, 3421–3435 (2014).
11. A. J. Teuling, S. I. Seneviratne, R. Stöckli, M. Reichstein, E. Moors, P. Ciais, S. Luyssaert, B. van den Hurk, C. Ammann, C. Bernhofer, E. Dellwik, D. Gianelle, B. Gielen, T. Grünwald, K. Klumpp, L. Montagnani, C. Moureaux, M. Sottocornola, G. Wohlfahrt, Contrasting response of European forest and grassland energy exchange to heatwaves. *Nat. Geosci.* **3**, 722–727 (2010).
12. A. G. Konings, P. Gentine, Global variations in ecosystem-scale isohydricity. *Glob. Chang. Biol.* **23**, 891–905 (2017).
13. S. Wolf, T. F. Keenan, J. B. Fisher, D. D. Baldocchi, A. R. Desai, A. D. Richardson, R. L. Scott, B. E. Law, M. E. Litvak, N. A. Brunsell, W. Peters, I. T. van der Laan-Luijkx, Warm spring reduced carbon cycle impact of the 2012 US summer drought. *Proc. Natl. Acad. Sci. U.S.A.* **113**, 5880–5885 (2016).
14. D. G. Miralles, A. J. Teuling, C. C. van Heerwaarden, J. Vila-Guerau de Arellano, Mega-heatwave temperatures due to combined soil desiccation and atmospheric heat accumulation. *Nat. Geosci.* **7**, 345–349 (2014).
15. W. Buermann, M. Forkel, M. O'Sullivan, S. Sitch, P. Friedlingstein, V. Haverd, A. K. Jain, E. Kato, M. Kautz, S. Lienert, D. Lombardozzi, J. E. M. S. Nabel, H. Tian, A. J. Wiltshire, D. Zhu, W. K. Smith, A. D. Richardson, Widespread seasonal compensation effects of spring warming on northern plant productivity. *Nature* **562**, 110–114 (2018).
16. G. Tramontana, M. Jung, C. R. Schwalm, K. Ichii, G. Camps-Valls, B. Ráduly, M. Reichstein, M. Altaf Arain, A. Cescatti, G. Kiely, L. Merbold, P. Serrano-Ortiz, S. Sickert, S. Wolf, D. Papale, Predicting carbon dioxide and energy fluxes across global FLUXNET sites with regression algorithms. *Biogeosci. Discuss.* 13, 4291–4313 (2016).
17. C. Albergel, E. Dutra, B. Bonan, Y. Zheng, S. Munier, G. Balsamo, P. de Rosnay, J. Muñoz-Sabater, J. C. Calvet, Monitoring and forecasting the impact of the 2018 summer heatwave on vegetation. *Remote Sens.* **11**, 520 (2019).
18. P. B. Cerlini, S. Meniconi, B. Brunone, Groundwater supply and climate change management by means of global atmospheric datasets. Preliminary results. *Procedia Eng.* **186**, 420–427 (2017).
19. A. Bastos, P. Friedlingstein, S. Sitch, C. Chen, A. Mialon, J.-P. Wigneron, V. K. Arora, P. R. Briggs, J. G. Canadell, P. Ciais, F. Chevallier, L. Cheng, C. Delire, V. Haverd, A. K. Jain, F. Joos, E. Kato, S. Lienert, D. Lombardozzi, J. R. Melton, R. Myneni, J. E. M. S. Nabel, J. Pongratz, B. Poulter, C. Rödenbeck, R. Séférian, H. Tian, C. van Eck, N. Viovy, N. Vuichard, A. P. Walker, A. Wiltshire, J. Yang, S. Zaehle, N. Zeng, D. Zhu, Impact of the 2015/2016 El Niño on the terrestrial carbon cycle constrained by bottom-up and top-down approaches. *Philos. Trans. R. Soc. B Biol. Sci.* **373**, 20170304 (2018).
20. M. G. De Kauwe, S.-X. Zhou, B. E. Medlyn, A. J. Pitman, Y.-P. Wang, R. A. Duursma, I. C. Prentice, Do land surface models need to include differential plant species responses to drought? Examining model predictions across a mesic-xeric gradient in Europe. *Biogeosciences* **12**, 7503–7518 (2015).
21. J. Sheffield, G. Goteti, F. Wen, E. F. Wood, A simulated soil moisture based drought analysis for the United States. *J. Geophys. Res. Atmos.* **109**, (2004).
22. M. Jung, C. Schwalm, M. Migliavacca, S. Walther, G. Camps-Valls, S. Koirala, P. Anthoni, S. Besnard, P. Bodesheim, N. Carvalhais, F. Chevallier, F. Gans, D. S. Goll, V. Haverd, P. Köhler, K. Ichii, A. K. Jain, J. Liu, D. Lombardozzi, J. E. M. S. Nabel, J. A. Nelson, M. O'Sullivan, M. Pallandt, D. Papale, W. Peters, J. Pongratz, C. Rödenbeck, S. Sitch, G. Tramontana, A. Walker, U. Weber, M. Reichstein, Scaling carbon fluxes from eddy covariance sites to globe: Synthesis and evaluation of the FLUXCOM approach. *Biogeosciences* **17**, 1343–1365 (2019).
23. J.-P. Wigneron, T. Jackson, P. O'neill, G. De Lannoy, P. De Rosnay, J. Walker, P. Ferrazzoli, V. Mironov, S. Bircher, J. P. Grant, M. Kurum, M. Schwank, J. Munoz-Sabater, N. Das, A. Royer, A. Al-Yaari, A. Al Bitar, R. Fernandez-Moran, H. Lawrence, A. Mialon, M. Parrens, P. Richaume, S. Delwart, Y. Kerr, Modelling the passive microwave signature from land surfaces: A review of recent results and application to the L-band SMOS & SMAP soil moisture retrieval algorithms. *Remote Sens. Environ.* **192**, 238–262 (2017).
24. R. Fernandez-Moran, A. Al-Yaari, A. Mialon, A. Mahmoodi, A. Al Bitar, G. De Lannoy, N. Rodriguez-Fernandez, E. Lopez-Baeza, Y. Kerr, J.-P. Wigneron, SMOS-IC: An alternative SMOS soil moisture and vegetation optical depth product. *Remote Sens.* **9**, 457 (2017).
25. M. Brandt, J.-P. Wigneron, J. Chave, T. Tagesson, J. Penuelas, P. Ciais, K. Rasmussen, F. Tian, C. Mbow, A. al-Yaari, N. Rodriguez-Fernandez, G. Schurgers, W. Zhang, J. Chang, Y. Kerr, A. Verger, C. Tucker, A. Mialon, L. V. Rasmussen, L. Fan, R. Fensholt, Satellite passive microwaves reveal recent climate-induced carbon losses in African drylands. *Nat. Ecol. Evol.* **2**, 827–835 (2018).
26. V. Haverd, B. Smith, L. Nieradzik, P. Briggs, W. Woodgate, C. Trudinger, J. G. Canadell, M. Cuntz, A new version of the CABLE land surface model (Subversion revision r4601) incorporating land use and land cover change, woody vegetation demography, and a novel optimisation-based approach to plant coordination of photosynthesis. *Geosci. Model Dev.* **11**, 2995–3026 (2018).
27. E. Joetzjer, C. Delire, H. Douville, P. Ciais, B. Decharme, D. Carrer, H. Verbeeck, M. de Weirdt, D. Bonal, Improving the $ISBA_{CC}$ land surface model simulation of water and carbon fluxes and stocks over the Amazon forest. *Geosci. Model Dev.* **8**, 1709–1727 (2015).
28. H. Tian, G. Chen, C. Lu, X. Xu, D. J. Hayes, W. Ren, S. Pan, D. N. Huntzinger, S. C. Wofsy, North American terrestrial CO_2 uptake largely offset by CH_4 and N_2O emissions: Toward a full accounting of the greenhouse gas budget. *Clim. Change* **129**, 413–426 (2015).
29. P. Meiyappan, A. K. Jain, J. I. House, Increased influence of nitrogen limitation on CO_2 emissions from future land use and land use change. *Global Biogeochem. Cycles* **29**, 1524–1548 (2015).
30. T. Mauritsen, J. Bader, T. Becker, J. Behrens, M. Bittner, R. Brokopf, V. Brovkin, M. Claussen, T. Crueger, M. Esch, I. Fast, S. Fiedler, D. Fläschner, V. Gayler, M. Giorgetta, D. S. Goll, H. Haak, S. Hagemann, C. Hedemann, C. Hohenegger, T. Ilyina, T. Jahns, D. Jimenéz-de-la-Cuesta, J. Jungclaus, T. Kleinen, S. Kloster, D. Kracher, S. Kinne, D. Kleberg, G. Lasslop, L. Kornblueh, J. Marotzke, D. Matei, K. Meraner, U. Mikolajewicz, K. Modali, B. Möbis, W. A. Müller, J. E. M. S. Nabel, C. C. W. Nam, D. Notz, S.-S. Nyawira, H. Paulsen, K. Peters, R. Pincus, H. Pohlmann, J. Pongratz, M. Popp, T. J. Raddatz, S. Rast, R. Redler, C. H. Reick, T. Rohrschneider, V. Schemann, H. Schmidt, R. Schnur, U. Schulzweida, K. D. Six, L. Stein, I. Stemmler, B. Stevens, J.-S. von Storch, F. Tian, A. Voigt, P. Vrese, K.-H. Wieners, S. Wilkenskjeld, A. Winkler, E. Roeckner, Developments in the MPI-M Earth System Model version 1.2 (MPI-ESM 1.2) and its response to increasing CO2. *J. Adv. Model. Earth Syst.* **11**, 998–1038 (2018).
31. B. Smith, D. Wårlind, A. Arneth, T. Hickler, P. Leadley, J. Siltberg, S. Zaehle, Implications of incorporating N cycling and N limitations on primary production in an individual-based dynamic vegetation model. *Biogeosciences* **11**, 2027–2054 (2014).
32. S. Lienert, F. Joos, A Bayesian ensemble data assimilation to constrain model parameters and land-use carbon emissions. *Biogeosciences* **15**, 2909–2930 (2018).
33. S. Zaehle, A. D. Friend, P. Friedlingstein, F. Dentener, P. Peylin, M. Schulz, Carbon and nitrogen cycle dynamics in the O-CN land surface model: 2. Role of the nitrogen cycle in the historical terrestrial carbon balance. *Global Biogeochem. Cycles* **24**, GB1006 (2010).
34. G. Krinner, N. Viovy, N. de Noblet-Ducoudré, J. Ogée, J. Polcher, P. Friedlingstein, P. Ciais, S. Sitch, I. C. Prentice, A dynamic global vegetation model for studies of the coupled atmosphere-biosphere system. *Global Biogeochem. Cycles* **19**, GB1015 (2005).
35. D. Zhu, S. Peng, P. Ciais, N. Viovy, A. Druel, M. Kageyama, G. Krinner, P. Peylin, C. Ottlé, S. L. Piao, B. Poutler, D. Schepaschenko, A. Shvidenko, Improving the dynamics of Northern Hemisphere high-latitude vegetation in the ORCHIDEE ecosystem model. *Geosci. Model Dev.* **8**, 2263–2283 (2015).
36. M. Guimberteau, D. Zhu, F. Maignan, Y. Huang, C. Yue, S. Dantec-Nédélec, C. Ottlé, A. Jornet-Puig, A. Bastos, P. Laurent, D. Goll, ORCHIDEE-MICT (revision 4126), a land surface model for the high-latitudes: Model description and validation. *Geosci. Model Dev.* **11**, 121–163 (2017).
37. A. P. Walker, T. Quaife, P. M. van Bodegom, M. G. De Kauwe, T. F. Keenan, J. Joiner, M. R. Lomas, N. MacBean, C. Xu, X. Yang, F. I. Woodward, The impact of alternative trait-scaling hypotheses for the maximum photosynthetic carboxylation rate (V_{cmax}) on global gross primary production. *New Phytol.* **215**, 1370–1386 (2017).
38. E. Dlugokencky, P. Tans, *Trends in Atmospheric Carbon Dioxide* (National Oceanic & National Oceanic & Atmospheric Administration, Earth System Research Laboratory, 2019).
39. G. Hurtt, L. P. Chini, S. Frolking, R. Betts, J. Feddema, G. Fischer, J. P. Fisk, K. Hibbard, R. A. Houghton, A. Janetos, C. D. Jones, G. Kindermann, T. Kinoshita, K. K. Goldewijk, K. Riahi, E. Shevliakova, S. Smith, E. Stehfest, A. Thomson, P. Thornton, D. P. van Vuuren, Y. P. Wang, Harmonization of land-use scenarios for the period 1500–2100: 600 years of global gridded annual land-use transitions, wood harvest, and resulting secondary lands. *Clim. Change* **109**, 117–161 (2011).
40. H. Tian, J. Yang, C. Lu, R. Xu, J. Canadell, R. Jackson, A. Arnet, J. Chang, G. Chen, P. Cais, S. Gerber, A. Ito, Y. Huang, F. Joos, S. Lienert, P. Messina, S. Olin, S. Pan, C. Peng, E. Saikawa, R. L. Thompson, N. Vuichard, W. Winiwarter, S. Zaehle, B. Zhang, K. Zhang, Q. Zhu, The global N_2O model intercomparison project. *Bull. Am. Meteorol. Soc.* **99**, 1231–1251 (2018).

Acknowledgments: We would like to thank C. Le Quéré and M. Jones for providing the CO_2 fields for 2018. The work was informally supported by the ICOS infrastructure. A.K.J. thanks S. Shu and E. Choi for their help in completing the ISAM model simulations. A.B. thanks J. Nabel for helpful comments about the experiment design. **Funding:** The ORCHIDEE and ORCHIDEE-MICT simulation was performed using HPC resources from GENCI-TGCC (grant 2018-A0050106328). S.L. has received funding from the European Union's Horizon 2020 research and innovation program under grant agreement no. 821003 (project 4C, Climate-Carbon Interactions in the Coming Century) and SNSF (grant no.

Downloaded from http://advances.sciencemag.org/ on July 27, 2020

20020_172476). P.F. received funding from the European Union's Horizon 2020 research and innovation program under grant agreement no. 821003 (4C). A.A. and P.A. were supported by the Helmholtz Association in its ATMO program. A.J. acknowledges the US Department of Energy (No. DE-SC0016323). **Author contributions:** A.B. conceived the study, preprocessed the climate forcing, performed the model simulations with ORCHIDEE-MICT, and analyzed the data. A.B. and P.C. prepared the manuscript draft. A.B., P.C., P.F., S.S., S.Z., M.R., and J.P. contributed to earlier stages of the study design and to the simulation protocol. L.F. and J.P.W. preprocessed and provided the L-VOD dataset. U.W., P.A., A.A., V.H., A.K.J., E.J., J.K., S.L., T.L., P.C.M., H.T., N.V., and S.Z. ran the DGVM simulations. All authors contributed to the manuscript revision. **Competing interests:** The authors declare that they have no competing interests. **Data and materials availability:** The ERA5 data can be downloaded from the Copernicus repository https://cds.climate.copernicus.eu. The outputs from the model simulations can be provided upon request to ana.bastos@lmu.de, S.A.Sitch@exeter.ac.uk, and P.Friedlingstein@exeter.ac.uk.

Submitted 19 November 2019
Accepted 14 April 2020
Published 10 June 2020
10.1126/sciadv.aba2724

Citation: A. Bastos, P. Ciais, P. Friedlingstein, S. Sitch, J. Pongratz, L. Fan, J. P. Wigneron, U. Weber, M. Reichstein, Z. Fu, P. Anthoni, A. Arneth, V. Haverd, A. K. Jain, E. Joetzjer, J. Knauer, S. Lienert, T. Loughran, P. C. McGuire, H. Tian, N. Viovy, S. Zaehle, Direct and seasonal legacy effects of the 2018 heat wave and drought on European ecosystem productivity. *Sci. Adv.* **6**, eaba2724 (2020).

Downloaded from http://advances.sciencemag.org/ on July 27, 2020

Science Advances

Direct and seasonal legacy effects of the 2018 heat wave and drought on European ecosystem productivity

A. Bastos, P. Ciais, P. Friedlingstein, S. Sitch, J. Pongratz, L. Fan, J. P. Wigneron, U. Weber, M. Reichstein, Z. Fu, P. Anthoni, A. Arneth, V. Haverd, A. K. Jain, E. Joetzjer, J. Knauer, S. Lienert, T. Loughran, P. C. McGuire, H. Tian, N. Viovy and S. Zaehle

Sci Adv **6** (24), eaba2724.
DOI: 10.1126/sciadv.aba2724

ARTICLE TOOLS http://advances.sciencemag.org/content/6/24/eaba2724

SUPPLEMENTARY MATERIALS http://advances.sciencemag.org/content/suppl/2020/06/08/6.24.eaba2724.DC1

REFERENCES This article cites 37 articles, 2 of which you can access for free
http://advances.sciencemag.org/content/6/24/eaba2724#BIBL

PERMISSIONS http://www.sciencemag.org/help/reprints-and-permissions

Use of this article is subject to the Terms of Service

Science Advances (ISSN 2375-2548) is published by the American Association for the Advancement of Science, 1200 New York Avenue NW, Washington, DC 20005. The title *Science Advances* is a registered trademark of AAAS.

Copyright © 2020 The Authors, some rights reserved; exclusive licensee American Association for the Advancement of Science. No claim to original U.S. Government Works. Distributed under a Creative Commons Attribution NonCommercial License 4.0 (CC BY-NC).

Downloaded from http://advances.sciencemag.org/ on July 27, 2020